Computer Modeling in Engineering & Sciences

Tech Science Press

DOI: 10.32604/cmes.2023.030508

ARTICLE

An 8-Node Plane Hybrid Element for Structural Mechanics Problems Based on the Hellinger-Reissner Variational Principle

Haonan Li[1], Wei Wang[2], Quan Shen[1] and Linquan Yao[1,*]

[1]School of Rail Transportation, Soochow University, Suzhou, 215131, China

[2]Soochow College, Soochow University, Suzhou, 215006, China

*Corresponding Author: Linquan Yao. Email: lqyao@suda.edu.cn

Received: 10 April 2023 Accepted: 18 July 2023 Published: 17 November 2023

ABSTRACT

The finite element method (FEM) plays a valuable role in computer modeling and is beneficial to the mechanical design of various structural parts. However, the elements produced by conventional FEM are easily inaccurate and unstable when applied. Therefore, developing new elements within the framework of the generalized variational principle is of great significance. In this paper, an 8-node plane hybrid finite element with 15 parameters (PH-Q8-15β) is developed for structural mechanics problems based on the Hellinger-Reissner variational principle. According to the design principle of Pian, 15 unknown parameters are adopted in the selection of stress modes to avoid the zero energy modes. Meanwhile, the stress functions within each element satisfy both the equilibrium and the compatibility relations of plane stress problems. Subsequently, numerical examples are presented to illustrate the effectiveness and robustness of the proposed finite element. Numerical results show that various common locking behaviors of plane elements can be overcome. The PH-Q8-15β element has excellent performance in all benchmark problems, especially for structures with varying cross sections. Furthermore, in bending problems, the reasonable mesh shape of the new element for curved edge structures is analyzed in detail, which can be a useful means to improve numerical accuracy.

KEYWORDS

8-node plane hybrid element; Hellinger-Reissner variational principle; locking behaviors; structural mechanics problems

1 Introduction

The FEM is a computational tool for engineering design analysis; it fundamentally revolutionized the way we perform scientific modeling and engineering design, including automobiles, aircraft, marine structures, bridges, highways, and high-rise buildings [1–9]. Traditional isoparametric elements are often limited by various numerical problems, such as limited computational accuracy and sensitivity to mesh distortion. For instance, the accuracy of the 4-node isoparametric element (Q4) may be obviously limited for bending problems due to shear locking. To improve the performance of these finite element methods, new finite element formulations need to be derived and applied to mechanical problems.

Over the past few decades, numerous techniques have been proposed for developing new finite element models based on various generalized variational principles. Pian et al. [10,11] pioneered the hybrid element method using an assumed stress field in the element and an assumed displacement field along element boundaries. Cen et al. [12] improved on Pian's hybrid element approach to develop 8- and 12-node plane elements. The new elements perform well and can work in highly distorted meshes. Sze et al. [13–18] developed a hybrid stress-assumed natural strain 8-node solid shell element unaffected by shear, membrane, trapezoidal, thickness, and dilatational locking. This element is computationally more efficient than conventional hybrid elements because it adopts orthogonal assumed stress modes and enforces admissible sparsity in the flexibility matrix. Moreover, this element was generalized for smart structure modeling by the piezoelectric effect. Jog et al. [19] presented 4-node and 9-node elements for the development of hybrid axisymmetric elements based on the Hellinger-Reissner principle within the context of linear elasticity. Several examples were presented to show the excellent performance of both elements in various situations. Ma et al. [20] proposed a 24 degree of freedom (DOF) quadrilateral hybrid stress element for couple stress theory. Reduced integration and a stress smoothing technique were introduced to improve the accuracy of this element. Numerical results showed that this element could pass the enhanced patch test for a convergence condition. Bussamra et al. [21] proposed hexahedral hybrid-mixed finite elements for free vibration analysis of three-dimensional solids. These elements were free of shear and volumetric locking and had low sensitivity to mesh distortion. Agrawal et al. [22] used hybrid finite element methodology to develop an efficient and robust method based on the Hellinger-Reissner variational principle towards developing an efficient and robust finite element-based contact strategy. The proposed contact formulation can effectively model the contact interaction of thin as well as thick geometries as well as contact between bodies made of almost incompressible materials. Xie et al. [23] developed an atomistic-informed crystal plasticity finite element method to capture the evolution of geometrically compatible dislocation patterns as well as crystal plasticity in body-centered cubic crystals at micron or submicron scales. Liu et al. [24] established a novel three-dimensional progressive damage model based on the generalized mixed finite element method to investigate the strength and failure behaviors of notched composite laminate plates. The stress distribution of notched isotropic plates under tension was studied, and the results verified the good accuracy of the method. Ping and co-workers [25–27] used a specific finite element eigen-analysis method to predict the singular stress field around the tips of cracks, notches, and inclusions within the framework of the Hellinger-Reissner variational principle. Based on this, they [28] proposed an adaptive FEM to examine the issues with fracture propagation in anisotropic materials, bi-materials, and isotropic materials. Ramtekkar et al. [29] developed a refined 6-node two-dimensional mixed finite element to analyze a laminated composite using the minimum potential energy principle. The results obtained through the model showed excellent agreement with the elastic solution. Additionally, smoothed FEMs can also increase numerical solution accuracy, and the core idea behind this method is to combine the strain smoothing methodology of meshfree methods into the standard finite element method [30–32]. According to [33,34], smoothed FEMs can be viewed as specific assumed strain or stress methods for generalized variational principles.

The quadrilateral isoparametric elements contain Lagrangian elements and Serendipity elements. The Lagrangian elements are more computationally expensive than the Serendipity elements since they contain internal nodes. Thus, the Serendipity elements are preferred in practical applications, especially the 8-node isoparametric element (Q8). As the biquadratic interpolation functions are adopted for the Q8 element, it has better accuracy compared with the Q4 element and the Wilson-incompatible element. However, the Q8 element is extremely sensitive to mesh distortion [35]. The design of 8-node plane elements that can both improve the accuracy and overcome the above

shortcomings has been a research hotspot. Dhananjaya et al. [36] presented a new 8-node Serendipity quadrilateral plate bending element based on Mindlin-Reissner theory using the integrated force method. This new element performs excellently in both thin and moderately thick plate bending situations. Dang et al. [37] presented a hybrid element model derived from a two-field variational functional; the plausible equilibrated stress field within each element was derived using Airy's stress functions. The results indicated that this hybrid element was less sensitive to geometric distortion and was more accurate for stress than standard finite elements. Wang et al. [38,39] derived a new 8-node assumed stress quasi-conforming plane element based on the Bernstein basis function and Airy's stress function. This element was not affected by mesh distortions and could adjust to the mesh shape, which deformed into a triangle or concave quadrangle with curved elements. However, derivations of 8-node plane hybrid elements for solving structural mechanics problems based on the Hellinger-Reissner variational principle have rarely been reported in previous literature. In this paper, the formulation of the PH-Q8-15β element is derived based on the Hellinger-Reissner variational principle, and the new element is tested and verified by numerical examples.

The outline of this paper is as follows. In Section 2, a new 8-node plane hybrid finite element is proposed based on the Hellinger-Reissner variational principle, and subsequently, the finite element formulation is derived. Numerical examples with results and discussions are presented in Section 3. Finally, a brief conclusion is presented in Section 4.

2 Finite Element Equations of the 8-Node Hybrid Element

2.1 The Hellinger-Reissner Variational Principle

Consider a linear elastic body with volume Ω in the Cartesian coordinate system. The domain boundary is denoted by $\partial\Omega = \partial\Omega u \bigcup \partial\Omega\sigma$, where $\partial\Omega u$ and $\partial\Omega\sigma$ are boundaries over which the displacements and tractions are prescribed, respectively. When the elastic body is in static equilibrium subjected to external forces, the following relationships are satisfied:

The equilibrium equation

$$\sigma_{ij,j} + \overline{P}_i = 0 \quad \text{in} \quad \Omega, \tag{1}$$

The strain–displacement relationship

$$\varepsilon_{ij} = \frac{1}{2}\left(u_{i,j} + u_{j,i}\right) \quad \text{in} \quad \Omega, \tag{2}$$

The constitutive relationship

$$\varepsilon_{ij} = \frac{\partial\psi}{\partial\sigma_{ij}} = S_{ijkl}\sigma_{kl} \quad \text{in} \quad \Omega, \tag{3}$$

The Neumann condition

$$\sigma_{ij}n_j = \overline{T}_i \quad \text{on} \quad \partial\Omega_\sigma, \tag{4}$$

The Dirichlet condition

$$u_i = \overline{u}_i \quad \text{on} \quad \partial\Omega_u. \tag{5}$$

where σ_{ij} and ε_{ij} represent the components of the stress tensor and strain tensor, respectively; u_i is the component of the displacement vector; $\overline{P}_i$ and $\overline{T}_i$ are the known load distributions in Ω and along the boundary $\partial\Omega_\sigma$, respectively; n_j is the component of the outwards unit normal vector; S_{ijkl} is the flexibility tensor; and the complementary energy density ψ is expressed as:

$$\psi = \int_0^{\sigma_{ij}} \varepsilon_{ij} \mathrm{d}\sigma_{ij}, \tag{6}$$

Then, Eqs. (1)–(5) can be expressed in terms of two independent fields, u_i and σ_{ij}, by the complementary energy principle and the Lagrangian multiplier method:

$$\Pi_{HR} = \int_\Omega \left[-\psi\left(\sigma_{ij}\right) + \frac{1}{2}\sigma_{ij}\left(u_{i,j} + u_{j,i}\right) - \overline{P}_i u_i \right] \mathrm{d}\Omega - \int_{\partial\Omega_\sigma} \overline{T}_i u_i \mathrm{d}\Gamma - \int_{\partial\Omega_u} \sigma_{ij} n_j \left(u_i - \overline{u}_i\right) \mathrm{d}\Gamma, \tag{7}$$

The domain of the elastic body is divided into n elements. Generally, the trial solution of displacement u_i in Eq. (7) is compatible within the entire domain of the elastic body, and the stress trial solution σij is allowed to be piecewise continuous. We can define the energy functional from Eq. (7) as the sum of the individual elements,

$$\Pi_{HR} = \sum_n \Pi_{HR}^e = \sum_n \left\{ \int_{\Omega^e} \left[-\psi\left(\sigma_{ij}\right) + \frac{1}{2}\sigma_{ij}\left(u_{i,j} + u_{j,i}\right) - \overline{P}_i u_i \right] \mathrm{d}\Omega^e - \int_{\partial\Omega_\sigma^e} \overline{T}_i u_i \mathrm{d}\Gamma \right\}, \tag{8}$$

where Ω^e is the domain of an element e.

The stationary condition of Eq. (8) is:

$$\delta\Pi_{HR} = 0. \tag{9}$$

2.2 Interpolation Functions of Variable Fields in Elements

A standard 8-node element in the natural coordinate system is shown in Fig. 1a, and a curved edge element after the isoparametric transformation in the Cartesian coordinate system is shown in Fig. 1b. For isoparametric elements, the interpolation functions of the coordinates and displacements are the same, i.e.,

$$\mathbf{X}\left(\xi, \eta\right) = \mathbf{N}\mathbf{X}^e, \tag{10}$$

$$\mathbf{U}\left(\xi, \eta\right) = \mathbf{N}\mathbf{q}^e, \tag{11}$$

where $\mathbf{X} = \left(x^e, y^e\right)^{\mathrm{T}}$ is the coordinate matrix; $\mathbf{X}^e = \left(x_1^e, y_1^e, \cdots, x_8^e, y_8^e\right)^{\mathrm{T}}$ is the node coordinate vector; $\mathbf{U} = \left(u^e, v^e\right)^{\mathrm{T}}$ is the displacement matrix; $\mathbf{q}^e = \left(u_1^e, v_1^e, \cdots, u_8^e, v_8^e\right)^{\mathrm{T}}$ is the node displacement vector; and the shape function matrix $\mathbf{N}$ can be expressed as:

$$\mathbf{N}\left(\xi, \eta\right) = \left[N_1\mathbf{I}_2, N_2\mathbf{I}_2, N_3\mathbf{I}_2, N_4\mathbf{I}_2, N_5\mathbf{I}_2, N_6\mathbf{I}_2, N_7\mathbf{I}_2, N_8\mathbf{I}_2\right], \tag{12}$$

where $\mathbf{I}_n$ is the n-th order identity matrix, and the shape functions are:

$$\begin{cases} N_i = \dfrac{1}{4}\left(1 + \xi_i\xi\right)\left(1 + \eta_i\eta\right)\left(\xi_i\xi + \eta_i\eta - 1\right) \quad \left(i = 1, 2, 3, 4\right), \\ N_i = \dfrac{1}{2}\left(1 - \xi^2\right)\left(1 + \eta_i\eta\right) \quad \left(i = 5, 7\right), \\ N_i = \dfrac{1}{2}\left(1 - \eta^2\right)\left(1 + \xi_i\xi\right) \quad \left(i = 6, 8\right). \end{cases} \tag{13}$$

where $\left(\xi_i, \eta_i\right)$ is the coordinate values of the i point.

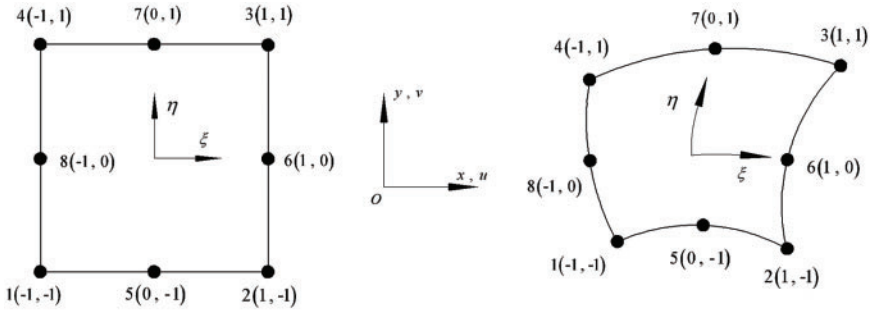

(a). Standard element (b). Curved quadrilateral element

Figure 1: Plane quadrilateral 8-node isoparametric element

The strain matrix can be obtained from Eq. (11):

$$\boldsymbol{\varepsilon} = \begin{pmatrix} \varepsilon_{xx} \\ \varepsilon_{yy} \\ \gamma_{xy} \end{pmatrix} = (\mathbf{LN})\,\mathbf{q}^e = \mathbf{B}\mathbf{q}^e, \tag{14}$$

where the geometric matrix $\mathbf{B}(x, y)$ can be expressed as:

$$\begin{aligned} \mathbf{B}(x, y) = \mathbf{LN} &= \begin{bmatrix} \dfrac{\partial}{\partial x} & 0 & \dfrac{\partial}{\partial y} \\ 0 & \dfrac{\partial}{\partial y} & \dfrac{\partial}{\partial x} \end{bmatrix}^{\mathrm{T}} [N_1\mathbf{I}_2, N_2\mathbf{I}_2, N_3\mathbf{I}_2, N_4\mathbf{I}_2, N_5\mathbf{I}_2, N_6\mathbf{I}_2, N_7\mathbf{I}_2, N_8\mathbf{I}_2] \\ &= [\mathbf{B}_1, \mathbf{B}_2, \mathbf{B}_3, \mathbf{B}_4, \mathbf{B}_5, \mathbf{B}_6, \mathbf{B}_7, \mathbf{B}_8], \end{aligned} \tag{15}$$

and $\mathbf{B}_i$ is given by:

$$\mathbf{B}_i = \begin{bmatrix} \dfrac{\partial N_i}{\partial x} & 0 & \dfrac{\partial N_i}{\partial y} \\ 0 & \dfrac{\partial N_i}{\partial y} & \dfrac{\partial N_i}{\partial x} \end{bmatrix}^{T} \quad (i = 1, 2, \cdots, 8). \tag{16}$$

The relationship between the natural coordinates (ξ, η) and the Cartesian coordinates (x, y) is as follows:

$$\begin{pmatrix} \dfrac{\partial}{\partial \xi} \\ \dfrac{\partial}{\partial \eta} \end{pmatrix} = \mathbf{J} \begin{pmatrix} \dfrac{\partial}{\partial x} \\ \dfrac{\partial}{\partial y} \end{pmatrix}, \tag{17}$$

where the Jacobi matrix $\mathbf{J}$ is given by:

$$\mathbf{J} = \begin{bmatrix} x_\xi & y_\xi \\ x_\eta & y_\eta \end{bmatrix} = \begin{bmatrix} \dfrac{\partial x}{\partial \xi} & \dfrac{\partial y}{\partial \xi} \\ \dfrac{\partial x}{\partial \eta} & \dfrac{\partial y}{\partial \eta} \end{bmatrix}. \tag{18}$$

In the hybrid element analysis, the performance of the elements constructed on the basis of different assumed stress fields differs. Therefore, the key to deriving a hybrid element with superior

performance lies in the selection of stress functions. Because the plane stresses are required to satisfy the continuity in each element, the stress functions are derived based on Eq. (1) by using the Airy stress function. To overcome the zero energy modes and ensure the efficiency of the calculation, it is necessary to determine the number of stress parameters and express them in n_β. For an 8-node plane hybrid element, its displacement DOF and rigid body DOF are expressed as $n_{q^e} = 16$ and $n_0 = 3$, respectively. We select 15 stress parameters in accordance with the theory presented in [40], $n_\beta \geq n_{q^e} - n_0$. The stress matrix is expressed as follows:

$$\boldsymbol{\sigma}(\xi,\eta) = \mathbf{P}\boldsymbol{\beta} = \mathbf{P}_{\mathrm{L}}\boldsymbol{\beta}_{\mathrm{L}} + \mathbf{P}_{\mathrm{H}}\boldsymbol{\beta}_{\mathrm{H}}, \tag{19}$$

where $\boldsymbol{\sigma} = (\sigma_{\xi\xi}, \sigma_{\eta\eta}, \sigma_{\xi\eta})^{\mathrm{T}}$ is the stress vector; $\mathbf{P}(\xi,\eta)$ and $\boldsymbol{\beta}$ are the stress function matrix and the stress parameter vector, respectively; $\boldsymbol{\beta}_{\mathrm{L}} = (\beta_1, \beta_2, \beta_3)^{\mathrm{T}}$ and $\boldsymbol{\beta}_{\mathrm{H}} = (\beta_4, \cdots, \beta_{15})^{\mathrm{T}}$ are the low-order stress parameter vector and the high-order stress parameter vector, respectively; $\mathbf{P}_{\mathrm{L}} = \mathbf{I}_3$ represents the third-order identity matrix; and the high-order stress matrix $\mathbf{P}_{\mathrm{H}}$ can be expressed as:

$$\mathbf{P}_{\mathrm{H}} = \begin{bmatrix} \xi & \eta & \xi\eta & \eta^2 & 0 & 0 & 0 & 0 & 0 & 0 & 0 & 0 \\ 0 & 0 & 0 & 0 & \xi & \eta & \xi\eta & \xi^2 & 0 & 0 & 0 & 0 \\ 0 & 0 & 0 & 0 & 0 & 0 & 0 & 0 & \xi & \eta & \xi^2 & \eta^2 \end{bmatrix}, \tag{20}$$

For a generic element, the stress function in the Cartesian coordinate system can be converted from Eq. (19) by the transformation matrix,

$$\boldsymbol{\sigma} = \mathbf{P}\boldsymbol{\beta} = \mathbf{P}_{\mathrm{L}}\boldsymbol{\beta}_{\mathrm{L}} + \mathbf{T}_{\mathrm{c}}\mathbf{P}_{\mathrm{H}}\boldsymbol{\beta}_{\mathrm{H}}, \tag{21}$$

where $\boldsymbol{\sigma} = (\sigma_{xx}, \sigma_{yy}, \sigma_{xy})$ T; the transformation matrix $\mathbf{T}_c$ is defined as:

$$\mathbf{T}_{\mathrm{c}} = \begin{bmatrix} x_\xi^2 & x_\eta^2 & 2x_\xi x_\eta \\ y_\xi^2 & y_\eta^2 & 2y_\xi y_\eta \\ x_\xi y_\xi & x_\eta y_\eta & x_\xi y_\eta + x_\eta y_\xi \end{bmatrix}_{\xi,\eta=0}. \tag{22}$$

Notably, the form of Eq. (20) obtained by using the Airy stress function is usually not unique. Eq. (20) possesses the advantages of good accuracy, good stability and strong universality in numerical examples. For special problems, such as fracture problems, more complex assumed stress functions can be used to construct the optimal element.

2.3 Derivation of the Finite Element Formulation

Substituting the displacement matrix $\mathbf{U}$, the strain matrix $\boldsymbol{\varepsilon}$ and the stress matrix $\boldsymbol{\sigma}$ into Eq. (9), we can obtain:

$$\Pi_{HR} = \sum_e \Pi_{HR}^e = \boldsymbol{\beta}^{\mathrm{T}}\mathbf{G}\mathbf{q}^e - \frac{1}{2}\boldsymbol{\beta}^{\mathrm{T}}\mathbf{H}\boldsymbol{\beta} - (\mathbf{q}^e)^{\mathrm{T}}\mathbf{Q}^e, \tag{23}$$

where $\mathbf{G} = \int_{\mathrm{A}^e} \mathbf{P}^{\mathrm{T}}(\mathbf{D}\mathbf{N})\, t\, \mathrm{dA}^e$, $\mathbf{H} = \int_{\mathrm{A}^e} (\mathbf{P}^{\mathrm{T}}\mathbf{S}\mathbf{P})\, t\, \mathrm{dA}^e$, and $\mathbf{Q}^e = \int_{\mathrm{A}^e} (\mathbf{N}^{\mathrm{T}}\overline{\mathbf{P}})\, t\, \mathrm{dA}^e + \int_{l^e} (\mathbf{N}^{\mathrm{T}}\overline{\mathbf{T}})\, t\, \mathrm{d}l^e$; t is the element thickness; $\overline{\mathbf{P}}$ and $\overline{\mathbf{T}}$ are the body load vector and the surface load vector, respectively. For plane stress problems, the flexibility matrix $\mathbf{S}$ is:

$$\mathbf{S} = \begin{pmatrix} \frac{1}{E} & -\frac{\mu}{E} & 0 \\ -\frac{\mu}{E} & \frac{1}{E} & 0 \\ 0 & 0 & \frac{(1-\mu)}{2} \end{pmatrix}. \tag{24}$$

where E is the Young's modulus and μ is the Poisson's ratio.

From the stationary condition of the energy functional, $\delta\Pi^{e}_{HR}(\boldsymbol{\beta}, \mathbf{q}^{e}) = 0$, the following equations can be obtained:

$$\mathbf{G}\mathbf{q}^{e} - \mathbf{H}\boldsymbol{\beta} = 0, \tag{25}$$

$$\mathbf{G}^{\mathrm{T}}\boldsymbol{\beta} - \mathbf{Q}^{e} = 0, \tag{26}$$

Eq. (25) imposes a strong geometric constraint on the displacement vector $\mathbf{q}^{e}$, whereas Eq. (26) imposes a weak equilibrium constraint on the stress parameter $\boldsymbol{\beta}$. As a result, the hybrid element is stiffened in two directions at the same time. In general, more parameters in Eq. (19) imply a better approximation. However, when $n_{\beta} \gg n_{q^e} - n_0$, the element stiffens to the point where locking behaviors may occur, so 15 parameters are a reasonable choice. It can be seen that the 15 stress modes chosen in Eq. (19) are independent of one another, and Zhang et al. [41] demonstrated that linear independence of assumed stress modes is a necessary and sufficient condition for the flexibility matrix $\mathbf{H}$ to be non-singular. As a result of Eq. (25), it follows that:

$$\boldsymbol{\beta} = \mathbf{H}^{-1}\mathbf{G}\mathbf{q}^{e}, \tag{27}$$

Substituting Eqs. (27) into (26), we obtain:

$$\left(\mathbf{G}^{\mathrm{T}}\mathbf{H}^{-1}\mathbf{G}\right)\mathbf{q}^{e} = \mathbf{K}^{e}\mathbf{q}^{e} = \mathbf{Q}^{e}, \tag{28}$$

where $\mathbf{K}^{e}$ is the stiffness matrix of the element.

By using Eqs. (23), (27) and (28), the energy functional of the elastic body can be expressed as:

$$\begin{aligned}\Pi_{HR} = \sum_{e}\Pi^{e}_{HR} &= \sum_{e}\left[-\frac{1}{2}\left(\mathbf{q}^{e}\right)^{\mathrm{T}}\mathbf{K}^{e}\mathbf{q}^{e} + \left(\mathbf{q}^{e}\right)^{\mathrm{T}}\mathbf{Q}^{e}\right] \\ &= -\frac{1}{2}\mathbf{q}^{\mathrm{T}}\mathbf{K}\mathbf{q} + \mathbf{q}^{\mathrm{T}}\mathbf{Q},\end{aligned} \tag{29}$$

where $\mathbf{K}$ is the stiffness matrix of the elastic body; $\mathbf{q}$ and $\mathbf{Q}$ are the displacement vector and the load vector of the node, respectively. From the variation of Eq. (29), we can obtain a set of algebraic equations:

$$\mathbf{K}\mathbf{q} = \mathbf{Q}. \tag{30}$$

After imposing displacement boundary conditions, the stiffness matrix $\mathbf{K}$ becomes non-singular, allowing the Eq. (30) to be solved. In general, the stiffness matrix $\mathbf{K}$ generated from the Hellinger-Reissner variational principle can be decomposed into a traditional stiffness with a reduced integration method and a higher-order stiffness, with the latter improving hybrid element computational efficiency and stability [42,43].

3 Numerical Examples

In this section, seven problems are presented to evaluate the performance of the PH-Q8-15β element. Several elements were taken from the literature for comparison, which are listed in Table 1. In the following, the geometric and physical parameters of each model are dimensionless, and the relative error is defined as:

$$Err = \left|\frac{\gamma - \gamma^{ref}}{\gamma^{ref}}\right|. \tag{31}$$

where γ and γ^{ref} are the numerical solution and the reference solution, respectively.

Table 1: List of elements for the comparison study

No.	Elements	Formulation methods
1	Q6	Traditional 6-node isoparametric element
2	Q8	Traditional 8-node isoparametric element
3	Q9	Traditional 9-node isoparametric element
4	PS	Quadrilateral 4-node hybrid element with 5 stress parameters
5	PS(a)	Penalty equilibrium hybrid element with 5 stress parameters
6	QACM8	8-node element using quadrilateral area coordinate
7	ATF-Q8	8-node hybrid plane element based on the complementary energy principle
8	HSF-Q8-15β	8-node hybrid plane quadrilateral element using the Airy stress function based on the complementary energy principle
9	QC-Q8-15β	8-node quasi-conforming plane element using the Airy stress function based on the complementary energy principle
10	QC-Q8-B	8-node quasi-conforming plane element using the Bernstein basis function based on the complementary energy principle
11	HR-Q9	9-node hybrid plane element based on the Hellinger-Reissner variational principle
12	MHR-Q9	9-node hybrid plane element based on the modified Hellinger-Reissner variational principle
13	NPB	Non prismatic beam model through dimensional reduction procedure based on the Hellinger-Reissner variational principle
14	TNCB	2-node curved beam element based on the exact analytical solution of the governing differential equation of planar curved beams

3.1 Patch Test

A rectangular panel ($0.24 \times 0.001 \times 0.12$) is divided into five irregular elements, as shown in Fig. 2. The material properties of the panel are Young's modulus $E = 1500$ and Poisson's ratio $\mu = 0.3$. The low- and high-order displacement fields given by Eqs. (32) and (33) are applied to the boundary nodes. The numerical results for the internal nodes in Fig. 2 are consistent with the analytical solutions, which demonstrates that the new element passes the patch test.

$$\begin{cases} u(x,y) = x + \dfrac{y}{2}, \\ v(x,y) = y + \dfrac{x}{2}, \end{cases} \tag{32}$$

$$\begin{cases} u(x,y) = \dfrac{1}{4} + x + 3\mathrm{y} - 2x^2 - 4xy + \dfrac{5}{2}y^2, \\ v(x,y) = 1 + \dfrac{x}{2} + 2y - \dfrac{2}{3}x^2 + \dfrac{17}{5}xy + \dfrac{3}{2}y^2. \end{cases} \tag{33}$$

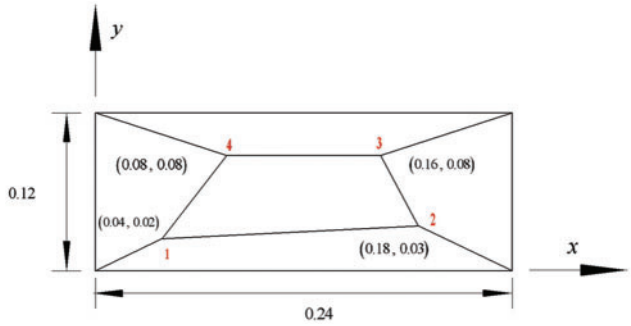

Figure 2: The patch test of membrane elements

3.2 Cantilever Beam with Five Irregular Elements

A cantilever beam with five irregular elements is subjected to the concentrated load F and bending moment M in Fig. 3. The geometry and material properties of the beam are as follows: length $L = 10$, height $h = 2$, width $b = 1$, Young's modulus $E = 1500$, and Poisson's ratio $\mu = 0.3$. Numerical results of the vertical deflection v_A at point A and the stress σ_{Bx} at point B are given in Tables 2 and 3. We find that compared with the traditional isoparametric elements, PS(a) element and QACM8 element, the PH-Q8-15β element has better accuracy.

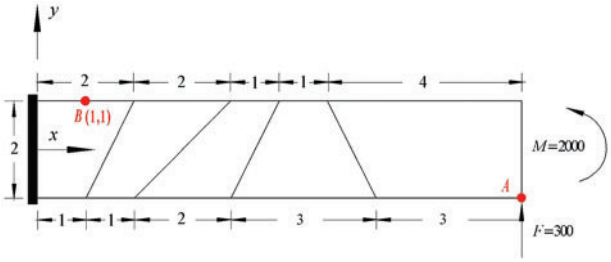

Figure 3: A cantilever beam with five irregular elements

Table 2: Numerical results of the displacement and stress at selected locations in the cantilever beam subjected to a bending moment M

Elements	v_A	*Err* (%)	σ_{Bx}	*Err* (%)
Q6 [44]	64.50	35.50	1515.00	49.50
Q8 [44]	99.70	0.30	2984.00	0.53
PS [40]	96.18	3.82	3014.00	0.47
PS(a) [40]	100.40	0.40	3000.00	0.00
QACM8 [44]	101.30	1.30	2920.00	2.67
PH-Q8-15β	99.99	0.01	3001.00	0.03
Analytical solution [44]	**100.00**		**3000.00**	

Table 3: Numerical results of the displacement and stress at selected locations in the cantilever beam subjected to a concentrated force F

Elements	v_A	*Err* (%)	σ_{Bx}	*Err* (%)
Q6 [44]	66.40	36.00	2923	27.83
Q8 [44]	101.50	2.17	4060	0.25
PS(a) [40]	100.90	0.90	4125	1.85
QACM8 [44]	102.70	1.01	3939	2.74
PH-Q8-15β	102.15	0.44	4084	0.84
Analytical solution [44]	**102.60**		**4050**	

3.3 Sensitivity Test for Mesh Distortion and Convergence Analysis

A cantilever beam is subjected to two different loads, as shown in Fig. 4. The beam is discretized using two elements, and e is the distortion parameter. The geometry and material properties of the beam are the same as those in Subsection 3.2. The normalized results of the vertical displacement v_A are listed in Tables 4 and 5. The tables show that the PH-Q8-15β element provides stable numerical solutions, even on distorted mesh shapes. Its stability is slightly less than that of the QC-Q8-B element.

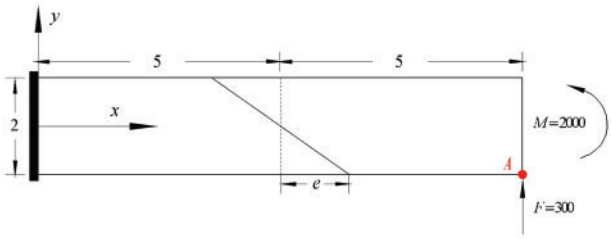

Figure 4: A cantilever beam divided by two elements with distortion parameter e

Table 4: The normalized results of the displacement for the cantilever beam subjected to a bending moment M

Elements	$e=0$	$e=1$	$e=2$	$e=3$	$e=4$	$e=4.9$
Q8 [44]	1.00	0.99	0.89	0.52	0.32	0.19
QACM8 [44]	1.00	1.00	1.00	1.02	1.04	1.00
ATF-Q8 [45]	1.00	1.00	1.00	1.00	1.00	1.00
QC-Q8-B [39]	1.00	1.00	1.00	1.00	1.00	1.00
PH-Q8-15β	1.00	1.00	1.00	1.00	0.98	0.96

Note: The standard value of v_A is 100.00.

Table 5: The normalized results of the displacement for the cantilever beam subjected to a concentrated force F

Elements	$e=0$	$e=1$	$e=2$	$e=3$	$e=4$	$e=4.9$
Q8 [44]	0.96	0.92	0.79	0.54	0.32	0.22
QACM8 [44]	0.96	0.94	0.87	0.84	0.84	0.85
ATF-Q8 [45]	0.99	0.98	0.97	0.95	0.89	0.69
QC-Q8-B [39]	0.99	0.98	0.97	0.96	0.93	0.80
PH-Q8-15β	0.97	0.97	0.95	0.90	0.88	0.86

Note: The standard value of v_A is 102.60.

We define the displacement norm error as follows in order to further analyze the convergence of the PH-Q8-15β element:

$$\delta_v = \frac{\|v - v_h\|_{H^0}}{\|v\|_{H^0}} = \frac{\left[\int_\Omega (v - v_h)^2 \, \mathrm{d}\Omega\right]^{\frac{1}{2}}}{\left(\int_\Omega v^2 \mathrm{d}\Omega\right)^{\frac{1}{2}}}, \tag{34}$$

where v and v_h are the vertical displacement and the approximated value of vertical displacement, respectively; $\|\cdot\|_{H^0}$ represents the norm defined on the Sobolev space.

The displacement norm error is calculated using a typical mesh type, as illustrated in Fig. 5. Numerical results are shown in Table 6. We can observe that the results for vertical displacement attain first order convergence.

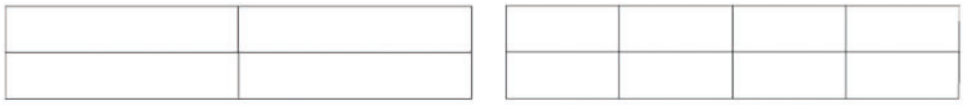

(a) 2×2 (b) 2×4

Figure 5: Typical mesh type models for convergence test

Table 6: Convergence results for different types of loads

Load type	The δ_v in different meshes				Order
	2×2	2×4	2×6	2×8	
F	0.1402	0.0592	0.0366	0.0262	1.20
M	0.1086	0.0401	0.0226	0.0152	1.38

3.4 Bending for a Curving Beam with the Uniform Cross Section

A curved cantilever beam subjected to a concentrated force F and the mesh shapes of the models are shown in Figs. 6 and 7, respectively. The geometric and physical parameters of the beam were selected from the literature for comparison [39]. For a thick curved beam, the geometry and material

properties are as follows: inner radius $R_i = 10$, middle radius $R_m = 12.5$, thickness $t = 5$, width $b = 1$, Young's modulus $E = 1000$, Poisson's ratio $\mu = 0.3$, and concentrated force $F = 600$. For a thin curved beam, the geometry and material properties are as follows: the inner radius $R_i = 4.12$, the middle radius $R_m = 4.22$, the thickness $t = 0.2$, the width $b = 0.1$, the Young's modulus $E = 10^6$, the Poisson's ratio $\mu = 0.25$, and the concentrated force $F = 1$. Based on the Castigliano energy theorem, the analytical solution of the radial displacement u_A for this problem is [46]:

$$u_A = \frac{\pi F R_m}{4}\left(\frac{R_m^2}{EI} + \frac{5}{6}\frac{1}{Gbt} + \frac{1}{Ebt}\right). \tag{35}$$

where R_m, t and b represent the middle radius, thickness and width, respectively; E is Young's modulus; the moment of inertia is $I = \frac{bh^3}{12}$; and the shear modulus is $G = \frac{E}{2(1+\mu)}$.

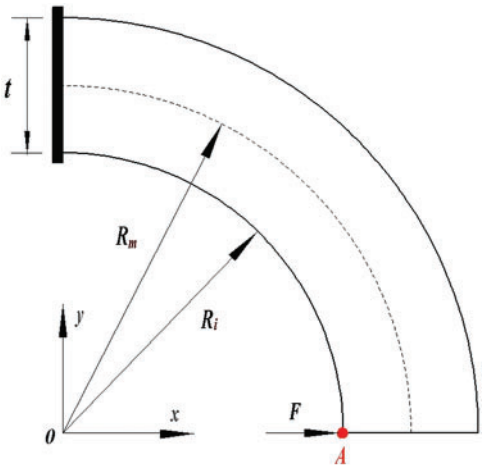

Figure 6: Curved cantilever beam

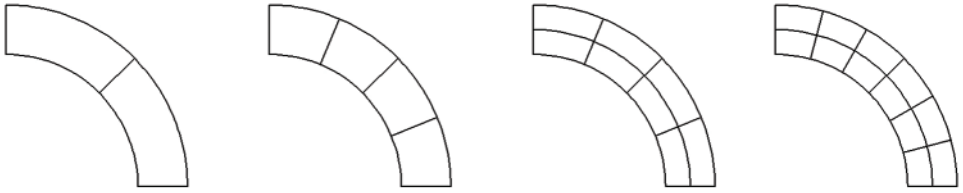

(a). 1×2 (b). 1×4 (c). 2×4 (d). 2×6

Figure 7: Typical mesh type models for the curved cantilever beam

Numerical results of the radial displacement u_A are listed in Tables 7 and 8. From the tables, we find that the results are more accurate for the new element than the other elements. Moreover, as the number of PH-Q8-15β elements increases, the double-layer mesh can improve the numerical accuracy of the thick curved beam. Therefore, the thin curved beam should be numerically calculated by the single-layer mesh.

Table 7: Results of u_A for the thick curved beam

Elements	Meshes							
	1 × 1	1 × 2	1 × 4	1 × 8	1 × 12	2 × 2	2 × 4	2 × 6
Q8 [44]	30.20	77.40	88.60	–	–	–	–	–
ATF-Q8 [45]	56.60	75.50	90.40	–	–	–	–	–
QC-Q8-15β [38]	52.49	90.15	90.55	–	–	–	–	–
QC-Q8-B [39]	65.10	88.93	90.32	–	–	–	–	–
PH-Q8-15β	85.75	96.71	92.80	92.97	92.95	90.63	91.85	92.20
Analytical solution	**92.08**							

Table 8: Results of u_A for the thin curved beam

Elements	Meshes							
	1 × 2	1 × 3	1 × 4	1 × 6	1 × 8	2 × 2	2 × 3	2 × 4
Q8 [44]	0.078	0.276	0.515	0.770	–	–	–	–
ATF-Q8 [45]	0.106	0.338	0.577	0.807				
QC-Q8-15β [38]	0.105	0.348	0.522	0.797	–	–	–	–
QC-Q8-B [39]	0.288	0.600	0.756	0.856	–	–	–	–
PH-Q8-15β	0.889	0.901	0.895	0.889	0.887	0.813	0.870	0.877
Analytical solution	**0.886**							

The effects of the mesh type on the numerical accuracy for the PH-Q8-15β element for different t/R_i ratios are investigated in Fig. 8. The vertical coordinate in the figures represents the relative error between the numerical results obtained by different meshes and the analytical solution for given t/R_i. The geometry and material properties are as follows: the inner radius $R_i = 10$, the width $b = 0.1$, the Young's modulus $E = 1000$, the Poisson's ratio $\mu = 0.3$, and the concentrated force $F = 1$. The figures show that when the value of t/R_i is close to 0.2, the single-layer mesh has better numerical accuracy, and it becomes more obvious with decreasing t/R_i. Therefore, when $t/R_i \leq 0.2$, the single-layer mesh should be preferred for a curved beam.

3.5 Locking Test

This test, proposed by Macneal and Harder, is a well-known benchmark for testing sensitivity to mesh distortion [47]. Three different mesh shapes in Fig. 9 are adopted: rectangular, parallelogram and trapezoidal. Two load types are considered: the bending moment and the concentrated force. The geometry and material properties are as follows: length $L = 6$, height $h = 0.2$, width $b = 0.1$, Young's modulus $E = 1500$, and Poisson's ratio $\mu = 0.3$. The normalized results of the vertical deflection v_A are listed in Table 9. Better and more accurate solutions can be obtained by the PH-Q8-15β element than by the other 8-node elements, and the PH-Q8-15β element can overcome shear and trapezoidal lockings.

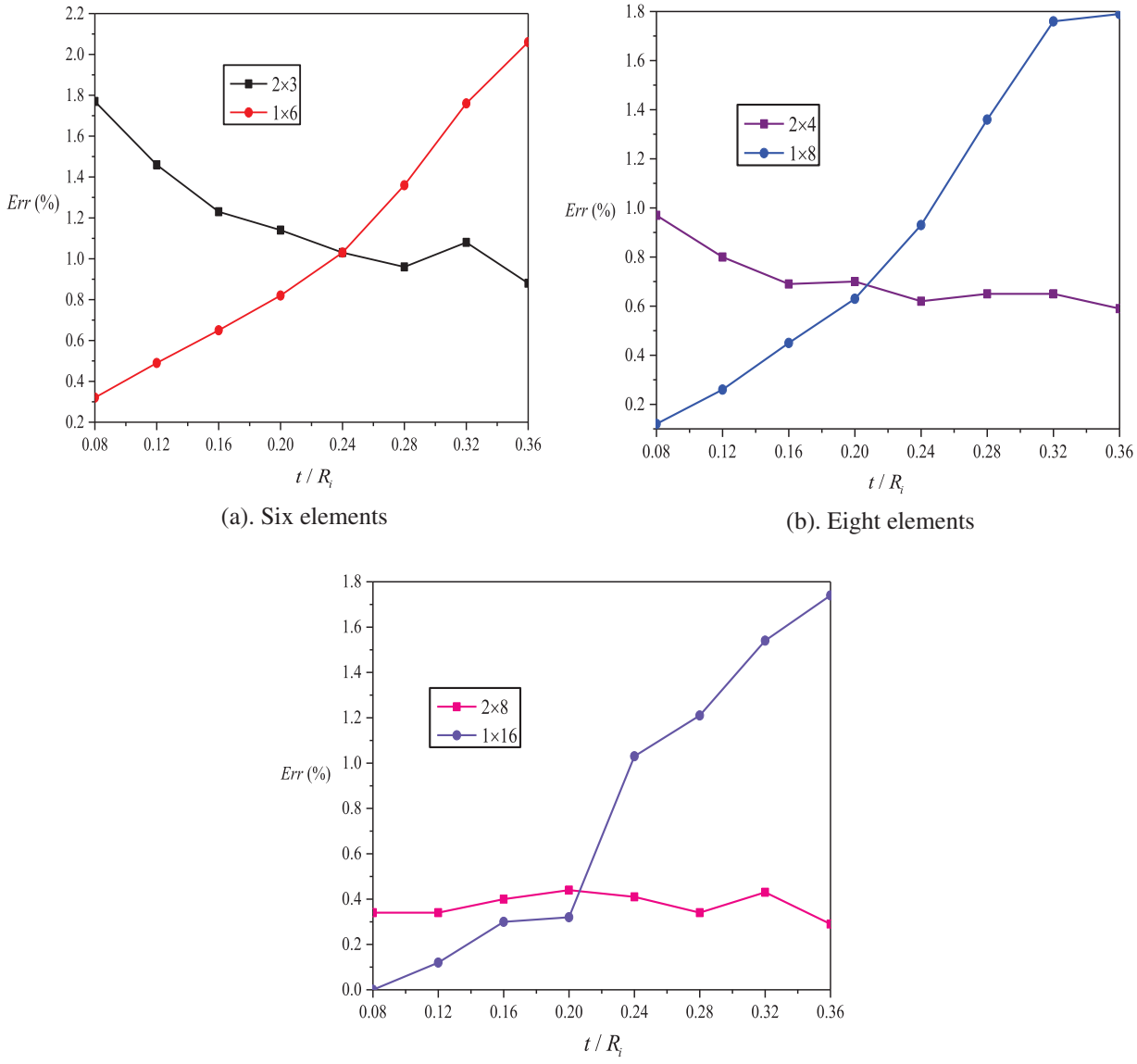

Figure 8: Influence of mesh type and t/R_i on the numerical accuracy of u_A for the curved beam

Additionally, shear locking can be alleviated by using bubble functions for a general plane stress problem; the functions are typically high-order displacement polynomials that are zero on the element boundaries [48,49]. This strategy, however, may improve the accuracy of elements with linear displacement modes (e.g., the Q4 element) but is not appropriate for the Q8 element. Because the Q8 element has a fully displacement mode that simulates the constant bending strain state.

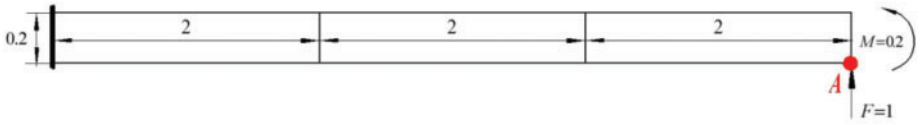

(a). Mesh 1

(b). Mesh 2

(c). Mesh 3

Figure 9: MacNeal thin beams

Table 9: The normalized results of the displacement for the MacNeal thin beam

Elements	Load M			Load F		
	Mesh 1	Mesh 2	Mesh 3	Mesh 1	Mesh 2	Mesh 3
Q8 [31]	0.951	0.919	0.854	1.000	0.994	0.939
Q9 [32]	0.974	0.939	0.942	1.000	1.000	1.000
QACM8 [31]	0.951	0.903	0.895	1.000	1.000	1.000
ATF-Q8 [32]	0.978	0.968	0.966	1.000	1.000	1.000
QC-Q8-B [29]	0.977	0.968	0.966	1.000	1.000	1.000
HSF-Q8-15β [12]	0.978	0.968	0.966	1.000	1.000	1.000
PH-Q8-15β	0.974	0.975	0.973	1.000	1.000	1.000

Note: [a]The standard value of v_A is 0.0054; [b]The standard value of v_A is 0.1081.

Membrane locking can be examined by the analysis of a ring, and many arch elements exhibit membrane locking in the analysis of deep arches even though they may give good results in the analysis of shallow arches [50]. A ring is subjected to two pinching concentrated loads F in Fig. 10a. Because of the symmetry, only a quarter of the ring is analyzed with appropriate boundary conditions in Fig. 10b. The geometry and material properties are as follows: inner radius $R_i = 5$, thickness $t = 0.1$, width $b = 0.1$, Young's modulus $E = 1 \times 10^7$, Poisson's ratio $\mu = 0.3$, and concentrated force $F = 1$.

According to the conclusion in Subsection 3.4, the single-layer mesh is adopted for the quarter of the thin pinched ring. Numerical results of the radial deflection v_A are listed in Table 10. The result obtained by eight PH-Q8-15β elements is consistent with the reference solution and converges to the reference solution quickly. Therefore, the PH-Q8-15β element can overcome membrane locking and can be successfully used to solve the pinched ring. We find that the numerical accuracy of the PH-Q8-15β element is lower than the HR-Q9 element and the MHR-Q9 element when the number of elements is 2.

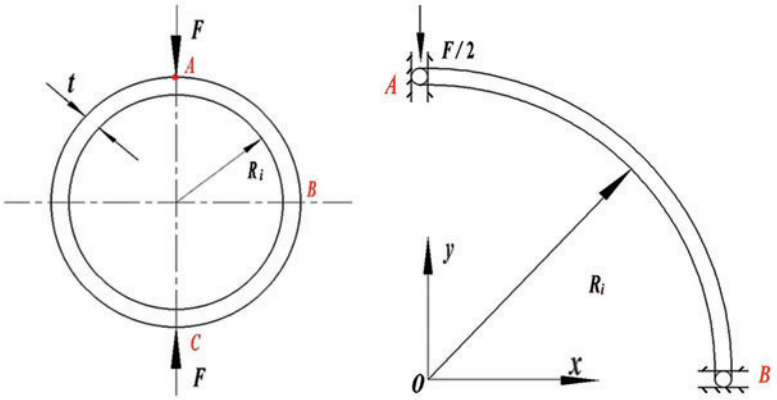

(a). The 2D model (b). The equivalent pinched ring model

Figure 10: Pinched ring

Table 10: Normalized results of v_A for the pinched ring

Elements	Meshes		
	1 × 2	1 × 4	1 × 8
HR-Q9 [51]	0.977	0.996	0.996
MHR-Q9 [51]	1.020	1.008	1.000
Q8	0.266	0.830	0.892
PH-Q8-15β	0.872	0.992	1.000

Note: The standard value of v_A is 0.00109.

Through the two examples in this subsection, it is evident that the proposed element has greatly improved the Q8 element and overcomes the common locking behaviors in plane stress problems. Meanwhile, when compared to other 8-node elements in the literature, better numerical accuracy was demonstrated.

3.6 Axisymmetric Annular Plate with Uniformly Distributed Internal Pressure

An axisymmetric annular plate is subjected to a uniformly distributed internal pressure q in Fig. 11a. The annular plate modelled by a quarter plate with appropriate boundary conditions is shown in Fig. 11b. The geometry and material properties are as follows: inner radius $R_i = 10$, outer radius $R_o = 15$, thickness $t = 0.1$, Young's modulus $E = 10^5$, Poisson's ratio $\mu = 0.3$, and internal pressure $q = 1$. The polar coordinate system is established at the central of the circular hole, and the analytical solutions of this problem for the radial stress σ_ρ and the hoop stress σ_θ can be expressed in Eq. (36):

$$\sigma_\rho = -\frac{\frac{R_o^2}{\rho^2} - 1}{\frac{R_o^2}{R_i^2} - 1} q, \quad \sigma_\varphi = \frac{\frac{R_o^2}{\rho^2} + 1}{\frac{R_o^2}{R_i^2} - 1} q. \tag{36}$$

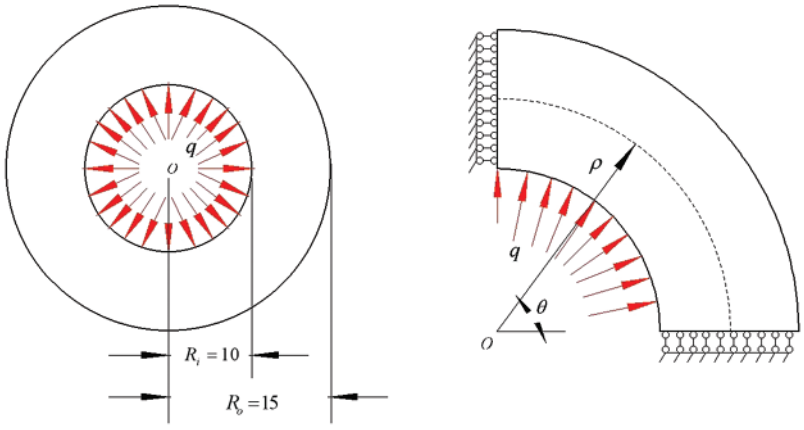

(a). The 2D model (b). The equivalent model

Figure 11: Axisymmetric annular plate with uniformly distributed internal pressure

The stress solutions of σ_ρ and σ_θ are functions of the variable ρ, independent of the angle θ. Fig. 12 shows the effects of the polar radius ρ and the number of elements on the radial stress σ_ρ and the hoop stress σ_θ, and the numerical results obtained by the PH-Q8-15β element are compared with the analytical solutions. With increasing ρ, the absolute values of σ_ρ and σ_θ gradually decrease, and the numerical results gradually converge to the analytical solutions with the increase in the number of elements. Therefore, the PH-Q8-15β element can be successfully used for this problem.

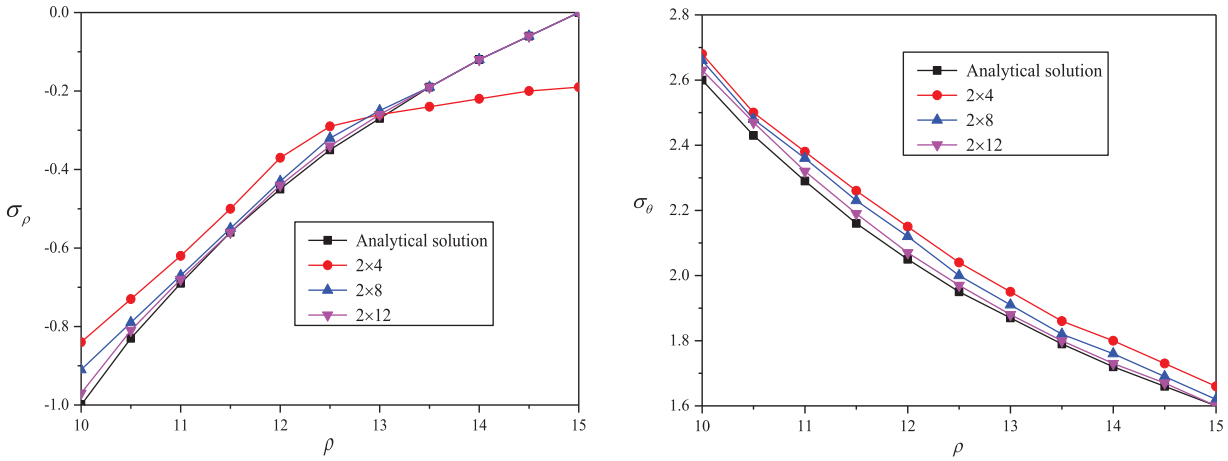

(a). The relationship between σ_ρ and ρ (b). The relationship between σ_θ and ρ

Figure 12: The variation in the radial stress σ_ρ and the hoop stress σ_θ relative to the polar radius ρ and number of elements for the axisymmetric annular plate

3.7 Straight/Curved Beams with Varying Cross Sections

A symmetric tapered beam is subjected to a concentrated load F in Fig. 13. The geometry and material properties are as follows: length $L = 10$, height of clamped end $h = 1$, height of cantilever end $h = 0.5$, width $b = 1$, Young's modulus $E = 10^5$, Poisson's ratio $\mu = 0.25$, and concentrated

force $F = 1$. Table 11 reports the numerical results of the vertical deflection v_A obtained by the PH-Q8-15β element and the NPB element. The "Axis Meshes" in Table 11 represent the number of evenly divided elements in the horizontal direction of the symmetric tapered beam. The table shows that the PH-Q8-15β element has better accuracy than the NPB element.

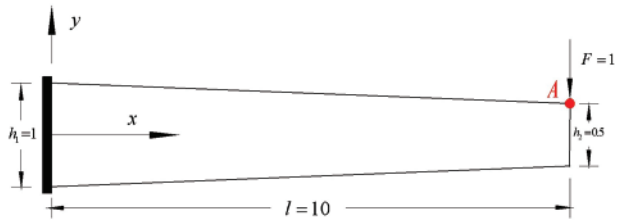

Figure 13: A symmetric tapered beam

Table 11: Results at selected location A that were obtained considering different axis meshes for the symmetric tapered beam subjected to a concentrated load F

Axis meshes	NPB [52]	PH-Q8-15β
1	−64.19e-3	−64.32e-3
4	−65.66e-3	−65.42e-3
20	−65.73e-3	−65.72e-3
Reference solution [52]	**−65.71e-3**	

A cantilever curving beam with a varying cross section is subjected to a concentrated load F in Fig. 14. The geometry and material properties are as follows: the middle radius $R_m = 5$, the thickness of the clamped end $t_1 = 0.6(1 + a)$, the thickness of the cantilever end $t_2 = 0.6(1 - a)$, where a is the taper ratio, the width $b = 0.4$, the Young's modulus $E = 3 \times 10^{10}$, the Poisson's ratio $\mu = 0.3$, and the concentrated force $F = 1$.

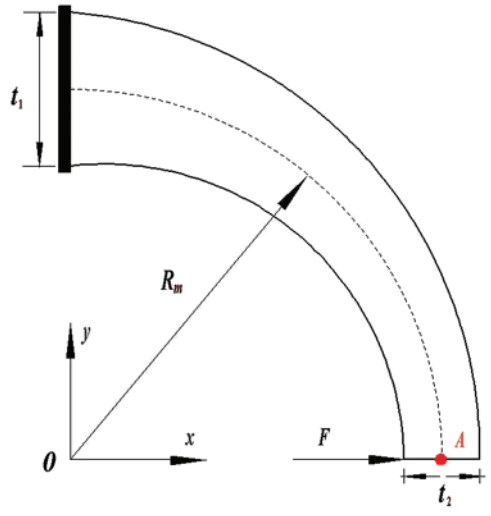

Figure 14: A curved beam with varying cross section

The single-layer mesh is adopted, as shown in Fig. 7. The results obtained by the 80 TNCB elements in [53] are taken as reference solutions and listed in Table 12. Fig. 15 shows the effects of the number of elements on the relative error between the numerical results obtained by the PH-Q8-15β element and the reference solution under different taper ratios a. The horizontal coordinate in figures represents the number of elements. We find that the PH-Q8-15β element can approximate the radial displacement u_A and the tangential displacement v_A with reasonable accuracy. Moreover, with the increase of the number of elements, the solution converges to the reference solution, which reflects the superior performance of the PH-Q8-15β element.

Table 12: Results of u_A and v_A for the curved beam with varying cross section

a	$u_A \times 10^{-5}$	$v_A \times 10^{-5}$
0.1	5.2168	3.1716
0.2	4.7893	2.7801
0.4	4.3172	2.2567

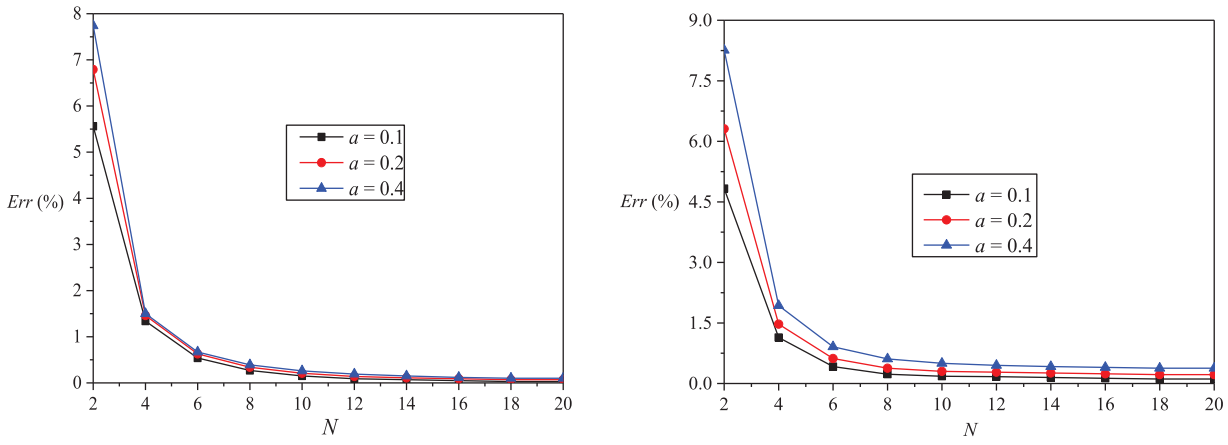

(a). Radial displacement u_A (b). Tangential displacement v_A

Figure 15: The variation in the relative error relative to the number of elements N for the curved beam with varying cross section

4 Conclusion

Because of the shortcomings of the Q8 element, a new PH-Q8-15β element is proposed for structural mechanics problems in this paper. We obtain the formulation of this element based on the Hellinger-Reissner variational principle. Fifteen unknown parameters are adopted in the selection of stress modes according to the design principle of Pian. Several numerical benchmark problems are presented to verify the performance of the PH-Q8-15β element. Numerical examples demonstrate that the PH-Q8-15β element has good accuracy and is not limited by various common locking behaviors of plane elements. Furthermore, the PH-Q8-15β element has better performance than the other elements in thin/thick curved beams with uniform cross sections. When the inner radius R_i of a curved beam is constant and $t/R_i \leq 0.2$, the curved beam should be modelled by a single-layer mesh. Finally,

the PH-Q8-15β element can be successfully applied to the problems of straight/curved beams with varying cross sections, and numerical results obtained with only a few elements are able to accurately approximate the reference solution.

In the future, we will extend the new PH-Q8-15β element to intelligent structures considering the flexoelectric effect and micromachinery and nanomachinery involving nonlocal strain gradient theory.

Acknowledgement: The authors would like to thank the editor and the reviewers for their constructive comments which improve the quality of the paper.

Funding Statement: This paper was supported by the National Natural Science Foundation of China (No. 11572210).

Author Contributions: The authors confirm contribution to the paper as follows: methodology and writing original draft: Haonan Li; investigation and software: Wei Wang; investigation and data curation: Quan Shen; validation and project administration: Linquan Yao. All authors reviewed the results and approved the final version of the manuscript.

Availability of Data and Materials: Data and materials will be made available by reasonable requests.

Conflicts of Interest: The authors declare that they have no conflicts of interest to report regarding the present study.

References

1. Liu, W. K., Li, S., Park, H. S. (2022). Eighty years of the finite element method: Birth, evolution, and future. *Archives of Computational Methods in Engineering, 29(6),* 4431–4453. https://doi.org/10.1007/s11831-022-09740-9
2. Truong, V. H., Liu, J., Meng, X. H., Jiang, C., Nguyen, T. T. (2018). Uncertainty analysis on vehicle-bridge system with correlative interval variables based on multidimensional parallelepiped model. *International Journal of Computational Methods, 15(5),* 1850030. https://doi.org/10.1142/S0219876218500305
3. Li, D., Tian, J., Shi, S., Wang, S., Deng, J. et al. (2023). Lightweight design of commercial vehicle cab based on fatigue durability. *Computer Modeling in Engineering & Sciences, 136(1),* 421–445. https://doi.org/10.32604/cmes.2023.024133
4. Wang, Y., Li, Z., Li, Z., Wang, Y. (2023). Finite element simulation of radial tire building and shaping processes using an elasto-viscoplastic model. *Computer Modeling in Engineering & Sciences, 135(2),* 1187–1208. https://doi.org/10.32604/cmes.2022.022596
5. Mehraban, A., Tufo, H., Sture, S., Regueiro, R. (2021). Matrix-free higher-order finite element method for parallel simulation of compressible and nearly-incompressible linear elasticity on unstructured meshes. *Computer Modeling in Engineering & Sciences, 129(3),* 1283–1303. https://doi.org/10.32604/cmes.2021.017476
6. Liu, H., Zhang, Q., Ma, J. (2021). Thermo-mechanical dynamics of two-dimensional FG microbeam subjected to a moving harmonic load. *Acta Astronautica, 178,* 681–692. https://doi.org/10.1016/j.actaastro.2020.09.045
7. van Vinh, P., Huy, L. Q. (2022). Finite element analysis of functionally graded sandwich plates with porosity via a new hyperbolic shear deformation theory. *Defence Technology, 18(3),* 490–508. https://doi.org/10.1016/j.dt.2021.03.006
8. Bach, D. P., Brancherie, D., Cauvin, L. (2022). An embedded-FEM approach accounting for the size effect in nanocomposites. *Computational Mechanics, 70(4),* 745–762. https://doi.org/10.1007/s00466-022-02194-7

9. Choi, M. J., Klinkel, S., Sauer, R. A. (2022). An isogeometric finite element formulation for frictionless contact of Cosserat rods with unconstrained directors. *Computational Mechanics, 70(6),* 71107. https://doi.org/10.1007/s00466-022-02223-5
10. Pian, T. H. H. (1964). Derivation of element stiffness matrices by assumed stress distributions. *AIAA Journal, 2(7),* 1333–1336. https://doi.org/10.2514/3.2546
11. Pian, T. H. H., Sumihara, K. (1984). Rational approach for assumed stress finite elements. *International Journal for Numerical Methods in Engineering, 20(9),* 1685–1695. https://doi.org/10.1002/nme.1620200911
12. Cen, S., Fu, X. R., Zhou, M. J. (2011). 8- and 12-node plane hybrid stress-function elements immune to severely distorted mesh containing elements with concave shapes. *Computer Methods in Applied Mechanics & Engineering, 200(29–32),* 2321–2336. https://doi.org/10.1016/j.cma.2011.04.014
13. Sze, K. Y., Yao, L. Q. (2000). A hybrid stress ANS solid-shell element and its generalization for smart structure modelling. Part I—Solid-shell element formulation. *International Journal for Numerical Methods in Engineering, 48,* 545–564.
14. Sze, K. Y., Yao, L. Q., Yi, S. (2000). A hybrid stress ANS solid-shell element and its generalization for smart structure modelling. Part II—Smart structure modelling. *International Journal for Numerical Methods in Engineering, 48,* 565–582.
15. Sze, K. Y., Yao, L. Q. (2000). Modelling smart structures with segmented piezoelectric sensors and actuators. *Journal of Sound and Vibration, 235(3),* 495–520. https://doi.org/10.1006/jsvi.2000.2944
16. Sze, K. Y., Lo, S. H., Yao, L. Q. (2002). Hybrid-stress solid elements for shell structures based upon a modified variational functional. *International Journal for Numerical Methods in Engineering, 53,* 2617–2642. https://doi.org/10.1002/nme.402
17. Sze, K. Y., Yao, L. Q., Pian, T. H. H. (2002). An eighteen-node hybrid-stress solid-shell element for homogenous and laminated structures. *Finite Elements in Analysis and Design, 38(4),* 353–374. https://doi.org/10.1016/S0168-874X(01)00089-0
18. Yao, L. Q., Lu, L. (2003). Hybrid-stabilized solid-shell model of laminated composite piezoelectric structures under non-linear distribution of electric potential through thickness. *International Journal for Numerical Methods in Engineering, 58,* 1499–1522. https://doi.org/10.1002/nme.823
19. Jog, C. S., Annabattula, R. (2006). The development of hybrid axisymmetric elements based on the Hellinger-Reissner variational principle. *International Journal for Numerical Methods in Engineering, 65,* 2279–2291. https://doi.org/10.1002/nme.1552
20. Ma, X., Chen, W. (2013). 24-DOF quadrilateral hybrid stress element for couple stress theory. *Computational Mechanics, 53(1),* 159–172. https://doi.org/10.1007/s00466-013-0899-7
21. Bussamra, F. L. S., Lucena Neto, E., Cardoso, F. R. (2018). Three-dimensional hybrid-mixed stress elements for free vibration analysis. *Finite Elements in Analysis and Design, 140(5–6),* 50–58. https://doi.org/10.1016/j.finel.2017.11.004
22. Agrawal, M., Nandy, A., Jog, C. S. (2019). A hybrid finite element formulation for large-deformation contact mechanics. *Computer Methods in Applied Mechanics & Engineering, 356(6),* 407–434. https://doi.org/10.1016/j.cma.2019.07.017
23. Xie, Y., Li, S. (2021). Finite temperature atomistic-informed crystal plasticity finite element modeling of single crystal tantalum (α-Ta) at micron scale. *International Journal for Numerical Methods in Engineering, 122,* 4660–4697. https://doi.org/10.1002/nme.6741
24. Liu, W., Yu, F., He, Z., Qing, G. (2020). A high-precision progressive damage model based on generalized mixed finite element method. *Archive of Applied Mechanics, 90(3),* 559–571. https://doi.org/10.1007/s00419-019-01625-x
25. Chen, M. C., Ping, X. C., Xie, H. M., Liu, Z. W. (2008). Numerical and experimental analyses of singular electro-elastic fields around a V-shaped notch tip in piezoelectric materials. *Engineering Fracture Mechanics, 75(18),* 5029–5041. https://doi.org/10.1016/j.engfracmech.2008.05.011

26. Ping, X. C., Chen, M. C., Zheng, B. B., Xu, B. (2013). An effective numerical analysis of singular stress fields in dissimilar material wedges under thermo-mechanical loads. *Engineering Fracture Mechanics, 106(17),* 22–37. https://doi.org/10.1016/j.engfracmech.2013.03.028
27. Ping, X. C., Wang, C. G., Cheng, L. P., Chen, M. C., Xu, J. Q. (2018). A super crack front element for three-dimensional fracture mechanics analysis. *Engineering Fracture Mechanics, 196(4),* 1–27. https://doi.org/10.1016/j.engfracmech.2018.04.016
28. Wang, C. M., Ping, X. C., Wang, X. X. (2023). An adaptive finite element method for crack propagation based on a multifunctional super singular element. *International Journal of Mechanical Sciences, 247(12),* 108191. https://doi.org/10.1016/j.ijmecsci.2023.108191
29. Ramtekkar, G. D., Patel, K. S., Desai, Y. M. (2023). A six-node refined mixed finite element model for the analysis of fiber reinforced polymer composite beams. *Composite Structures, 304(2),* 116418. https://doi.org/10.1016/j.compstruct.2022.116418
30. Liu, G. R., Nguyen-Thoi, T. (2010). *Smoothed finite element methods*. New York: CRC Press.
31. Nguyen, T. K., Nguyen, V. H., Thanh, C. D., Vo, T. P., Nguyen-Xuan, H. (2016). Static and vibration analysis of isotropic and functionally graded sandwich plates using an edge-based MITC3 finite elements. *Composites Part B: Engineering, 107(8),* 162–173. https://doi.org/10.1016/j.compositesb.2016.09.058
32. Lee, C., Kim, S., Lee, P. S. (2021). The strain-smoothed 4-node quadrilateral finite element. *Computer Methods in Applied Mechanics & Engineering, 373,* 113481. https://doi.org/10.1016/j.cma.2020.113481
33. Liu, G. R., Nguyen-Xuan, H., Nguyen-Thoi, T. (2010). A theoretical study on the smoothed FEM (S-FEM) models: Properties, accuracy and convergence rates. *International Journal for Numerical Methods in Engineering, 84(10),* 1222–1256. https://doi.org/10.1002/nme.2941
34. Lee, C., Park, J. (2021). A variational framework for the strain-smoothed element method. *Computers & Mathematics with Applications, 94,* 76–93. https://doi.org/10.1016/j.camwa.2021.04.025
35. Lee, N. S., Bathe, K. J. (1993). Effects of element distortions on the performance of isoparametric elements. *International Journal for Numerical Methods in Engineering, 36,* 3553–3576. https://doi.org/10.1002/nme.1620362009
36. Dhananjaya, H. R., Pandey, P. C., Nagabhushanam, J. (2009). New eight node serendipity quadrilateral plate bending element for thin and moderately thick plates using integrated force method. *Structural Engineering and Mechanics, 33(4),* 485–502. https://doi.org/10.12989/sem.2009.33.4.485
37. Dang, T. D., Hung, N. D. (2013). A hybrid element model for structural mechanics problems. *European Journal of Mechanics-A/Solids, 42(3),* 469–479. https://doi.org/10.1016/j.euromechsol.2013.08.001
38. Wang, C., Wang, Y., Yang, C., Zhang, X., Hu, P. (2017). 8-node and 12-node plane elements based on assumed stress quasi-conforming method immune to distorted mesh. *Engineering Computations, 34(8),* 2731–2751. https://doi.org/10.1108/EC-11-2016-0404
39. Wang, C., Lu, X., Zhang, X., Hu, P. (2018). 8-node quasi-conforming plane element by using Bernstein basis functions. *European Journal of Mechanics-A/Solids, 70(1–5),* 127–140. https://doi.org/10.1016/j.euromechsol.2018.02.003
40. Pian, T. H. H., Wu, C. C. (2006). *Hybrid and incompatible finite element methods*. New York: Chapman & Hall/CRC.
41. Zhang, C. H., Feng, W., Huang, Q. (2002). The stress subspace of hybrid stress element and the diagonalization method for flexibility matrix H. *Applied Mathematics and Mechanics, 23(11),* 1263–1273. https://doi.org/10.1007/BF02439457
42. Sze, K. Y. (2003). A novel approach for devising higher-order hybrid elements. *International Journal for Numerical Methods in Engineering, 36(19),* 3303–3316. https://doi.org/10.1002/nme.1620361907
43. Sze, K. Y., Yang, X. M., Yao, L. Q. (2004). Stabilized plane and axisymmetric piezoelectric finite element models. *Finite Elements in Analysis and Design, 40(9–10),* 1105–1122. https://doi.org/10.1016/j.finel.2003.06.002

44. Cen, S., Chen, X. M., Fu, X. R. (2007). Quadrilateral membrane element family formulated by the quadrilateral area coordinate method. *Computer Methods in Applied Mechanics & Engineering, 196(41–44),* 4337–4353. https://doi.org/10.1016/j.cma.2007.05.004
45. Fu, X. R., Cen, S., Li, C. F. (2010). Analytical trial function method for development of new 8-node plane element based on the variational principle containing Airy stress function. *Engineering Computations, 27(4),* 442–463. https://doi.org/10.1108/02644401011044568
46. Tayşi, N., Göğüş, M. T., Özakça, M. (2011). Structural analysis of arches in plane with a family of simple and accurate curved beam elements based on Mindlin-Reissner model. *Journal of Mechanics, 27(1),* 129–138. https://doi.org/10.1017/jmech.2011.14
47. Macneal, R. H., Harder, R. L. (1985). A proposed standard set of problems to test finite element accuracy. *Finite Elements in Analysis and Design, 1(1),* 3–20. https://doi.org/10.1016/0168-874X(85)90003-4
48. Kemp, B. L., Cho, C. M., Lee, S. W. (1998). A four-node solid shell element formulation with assumed strain. *International Journal for Numerical Methods in Engineering, 43(5),* 909–924. https://doi.org/10.1002/(SICI)1097-0207(19981115)43:5<909::AID-NME450>3.0.CO;2-X
49. Nassehi, V., Parvazinia, M. (2009). A multiscale finite element space-time discretization method for transient transport phenomena using bubble functions. *Finite Elements in Analysis and Design, 45(5),* 315–323. https://doi.org/10.1016/j.finel.2008.10.005
50. Shi, G., Voyiadjis, G. Z. (1991). Simple and efficient shear flexible two-node arch/beam and four-node cylindrical shell/plate finite elements. *International Journal for Numerical Methods in Engineering, 31,* 759–776. https://doi.org/10.1002/nme.1620310408
51. Sze, K. Y., Fan, H., Chow, C. L. (2010). Elimination of spurious pressure and kinematic modes in biquadratic nine-node plane element. *International Journal for Numerical Methods in Engineering, 38(23),* 3911–3932. https://doi.org/10.1002/nme.1620382302
52. Auricchio, F., Balduzzi, G., Lovadina, C. (2015). The dimensional reduction approach for 2D non-prismatic beam modelling: A solution based on Hellinger-Reissner principle. *International Journal of Solids and Structures, 63(12),* 264–276. https://doi.org/10.1016/j.ijsolstr.2015.03.004
53. Tufekci, E., Eroglu, U., Aya, S. A. (2017). A new two-noded curved beam finite element formulation based on exact solution. *Engineering with Computers, 33(2),* 261–273. https://doi.org/10.1007/s00366-016-0470-1